NUMERICAL ANALYSIS OF THE DETERMINISTIC STRESSES ASSOCIATED TO IMPELLER-TONGUE INTERACTIONS IN A SINGLE VOLUTE CENTRIFUGAL PUMP

Authors: Fernández Oro, J.M.; González, J.; Barrio Perotti, R.; Galdo Vega, M.

Universidad de Oviedo, Área de Mecánica de Fluidos.

Campus de Viesques. c/Wifredo Ricart s/n. 33203 Gijón, Asturias (Spain).

Corresponding author: Fernández Oro, J.M. E-mail: jesusfo@uniovi.es

Abstract.

In this paper, a deterministic stress decomposition is applied over the numerical 3D flow solution available for a single volute centrifugal pump. The numerical model has proven in previous publications its robustness to obtain the impeller to volute-tongue flow interaction and it is now used as starting point for the current research. The main objective has been oriented towards a detailed analysis of the lack of uniformity in the flow that the volute tongue promotes on the blade-to-blade axisymmetric pattern. Through this analysis, the fluctuation field may be retrieved and main interaction sources have been pinpointed.

The results obtained with the deterministic analysis becomes of paramount interest to understand the different flow features found in a typical centrifugal pump as a function of the flow rate. Moreover, this post-processing tool provides an economic and easy procedure for designers to compare the different deterministic terms; also giving relevant information on the unresolved turbulence intensity scales. Complementarily, a way to model the turbulent effects in a systematic way is also presented, comparing their impact on the performance with respect to deterministic sources in a useful framework, that may be applied for similar kind of pumps.

1. Introduction.

Centrifugal pumps are a type of turbomachine, quite widespread in modern industry and daily applications, used to deliver a given flow rate of an incompressible fluid, typically water, with a radial flow or centrifugal impeller arrangement. In the early stage of the research, the focus was set on global performance and several studies tried to explain the basic flow features, see for instance Binder et al. [1] or Bowerman et al. [2]. More advanced ideas were studied in Adkins et al. [3] or Miner et al. [4]. Also, global features were presented in Greitzer [5], Lakshminarayana [6] or Brennen [7].

More recently, investigations on centrifugal pumps have been focused on the understanding of the unsteady flow patterns and the interactions that show up in the different working conditions of the machine, being especially oriented towards the improvement of the final pump design. In other words, unsteady flow patterns are deeply analysed in the industrial day-to-day activity and in the bibliography due to their particular interest for obtaining new and better designs.

The experimental works with advanced measurement techniques have been also significantly developed over the years, leading to an extensive technical bibliography where the studies by Tsukamoto et al. [8] or Kaupert et al. [9] can be considered pioneering works within the field. The latter showed the unsteady pressure distributions inside the impeller of a centrifugal pump using piezoresistive transducers with the application of a telemetry system. Their study revealed quite high-pressure pulses, particularly at the blades trailing edge. Up to 35% of the pump head at off-design conditions was observed in the pressure side of the blades close to the trailing edge. In addition, concerning flow visualization techniques, the works by Dong et al. [10] or Wuibaut et al. [11] are also relevant references to be mentioned.

Concerning numerical studies, the number of numerical simulations, particularly those including 3D and full-unsteady flow descriptions, has been growing significantly since the initial

works by Croba and Kueny [12], Shi and Tsukamoto [13], Goto and Zangeneh [14] or González et al. [15]. Some other recent contributions have even handled some blade geometry changes in a very advanced way, see Wu et al. [16] among others.

All this knowledge is now available, and the databases provided by these works are a very solid base for the development of new advances. During the last years, pump designers have been stirred up in the search for more efficient and with less vibration prototypes. All those efforts pursuit a decrease of the pressure fluctuations in the volute, which becomes a key issue in the design objectives and promotes an iterative procedure that implies geometry changes until desired results are accomplished. Obviously, to have a deeper knowledge of the flow features and, particularly, of the pressure or velocity fluctuations, an indication of the origin and characteristics of the main interactions must be provided.

The deterministic flow decomposition was firstly defined as a modelling tool to address unsteady effects in steady simulations, see Adamczyk [17,18]. But, with the empowering of the computational resources, it became more a post-processing technique to analyse unsteady data in a coherent and more understandable way, Van Zante et al. [19]. Though it was originally conceived for multistage axial turbomachinery, the authors have already presented the application of this methodology for centrifugal pumps, see Fernández Oro et al. [20], advancing interesting features in the case of a double suction pump.

In this article, a deterministic stress analysis is performed for the flow in a typical, single-volute centrifugal pump. The location and strength of the main stress contributors, in terms of deterministic kinetic energy are obtained and compared to turbulent phenomena. By doing so, the sources of the main unsteadiness are identified along the geometry for the different working conditions of the pump.

2. Geometry: global description and numerical details.

A single stage centrifugal pump is being studied. It consists of an axial inlet at the suction section, a centrifugal impeller with seven logarithmic blades (concerning the mean line definition) and a volute, which collects the flow from the volute tongue towards the outlet section. Thus, the geometry can be regarded as a kind of classical geometrical arrangement for a single volute centrifugal pump (see Fig. 1).

Fig. 1. Global sketch of a typical centrifugal pump.

The performance curve of the pump, its nominal working point and the specific speed (n_S = 0.52) were extensively discussed in previous works. The reader is referred to González et al. [15], González et al. [21] and Parrondo et al. [22] for details. Also, a full description of the flow patterns was accomplished in González et al. [23], considering both the global variables and the vorticity distributions as sources of secondary flows along the volute.

Therefore, the considered pump has been extensively studied both in the numerical and experimental basis, considering both the nominal working conditions and off-design characteristics using full unsteady approaches. In particular, the work by Barrio et al. [24] provides a major contribution on the field by showing both steady and unsteady radial forces on the impeller, by integrating the instantaneous evolution of the pressure and viscous terms at different locations around the impeller exit for different flow rates. Fig. 2 shows the single volute commercial pump that has been used for all these research activities. Table 1 summarizes the relevant geometrical parameters and the nominal working conditions of the pump.

Fig. 2. Single volute commercial pump used for the present study.

Number of blades, Z (-)	7
Impeller outer diameter, D_2 (m)	0.2
Outlet blade angle, β_2 (deg.)	29
Impeller width, b_2 (m)	0.0169
Rotational speed, Ω (rpm)	1620
Nominal flow rate, Q_N (m³/s)	0.015
Head at nominal flow rate, H_N (m)	12.88
Specific speed, n_S (-)	0.52

Table 1. Main geometrical and operating variables.

3. Numerical 3D flow model.

A full 3D numerical model of the commercial pump has been developed. The model includes the impeller, the volute, the front and rear casing walls and also a short portion of the inlet and outlet pipes. The calculations of the flow through the pump have been carried out by solving the Unsteady Reynolds-Averaged Navier-Stokes equations (URANS) with a CFD commercial package, particularly the ®Ansys-Fluent. The numerical description, overall results and additional specific details on the pressure fields and their time description have been handled in Barrio et al. [24].

Fig. 3. General view of the numerical model.

Fig. 3 presents a general view of the model, where the inlet pipe, impeller and casing walls are shifted for clarity. The mesh used in the calculations was tetrahedral and unstructured except for the two pipes, where structured prismatic cells were adopted. Grid dependence tests showed that the adopted 800,000 cells were enough in order to keep numerical uncertainty below 4%. In addition, grid quality tests revealed that more than 90% of the cells had a magnitude of the equisize skew below 0.5. The impeller passages were discretized with 100 nodes streamwise, 35 nodes

pitchwise and 20 nodes to cover the impeller width, thus resulting in approx. 70,000 cells per passage. It is also remarkable that the number of cells required for a deterministic decomposition of the velocity field, like the one presented in following sections, is not as large as that usually needed for a detailed description of the viscous flow interactions. Details of the surface mesh of the impeller (including mesh refinement at the leading edge of the blades) and of the volute are shown in Fig. 4. An additional cut view with the 3D mesh in the vicinity of the tongue is provided.

The flow equations were discretized by second-order terms. Turbulent closure was established by means of the k-epsilon RNG turbulence model, together with the classic Log-law velocity profile to resolve the flow in the boundary layer. A full rotation of the impeller was computed in a sequence of 224 time steps by a Sliding Mesh Model (SMM), which resulted in a shift of 1.6 deg between two consecutive time steps. The boundary condition imposed at the inlet pipe was a constant gauge pressure. The mass flow was regulated by means of an outlet-vent boundary condition that was imposed at the outlet pipe. This condition simulates the operation of a regulation valve by means of a minor loss coefficient K. A series of values of K were determined from the experimental performance curve of the pump in order to obtain mass flows rated between 20% and 160% of the nominal one.

Fig. 4. Details of the surface mesh of the impeller (left) and volute (center). Transversal cut of the 3D mesh in the vicinity of the volute tongue (right).

The convergence criterion imposed during all calculations was to reach a magnitude of the scaled residuals below 10^{-5} for all the flow variables. About 10 to 15 full impeller revolutions were required to achieve a periodic flow regime. After that, an additional blade passage was computed and stored to obtain and analyse the results presented in the following sections.

4. Deterministic analysis framework.

4.1. General ideas on the velocity decomposition

The basis for a deterministic decomposition of the velocity field in a single-stage unsteady environment is firstly outlined in this section. Its application will allow to numerically split the effect of the different unsteadiness inside the pump, providing information on the origin of the losses and a deeper knowledge of the flow structures inside the pump. The main idea behind the whole procedure relies on the way the final velocity field is obtained from the superposition of deterministic and non-deterministic components. As a starting point, a first time-averaging operator has to be introduced according to:

$$\bar{u}_i(\vec{x}) = \frac{1}{T_B}\int_0^{T_B} \tilde{u}_i(\vec{x},t)dt \approx \frac{1}{N}\sum_{n=1}^{N} \tilde{u}_i(\vec{x},t_n) \qquad (1)$$

With N being the total number of time steps covering a blade element (i.e., the time required for a blade to complete a tangential movement comprising the pitch of the blade passage). Note that $\tilde{u}_i(\vec{x},t_n)$ has been previously obtained as the ensemble-averaging value of the instantaneous velocity, thus removing all turbulent scales (this is immediate within the URANS solution of the flow field). The deterministic fluctuation, $u_i'(\vec{x},t_n)$, can be calculated as the difference between $\bar{u}_i(\vec{x})$ and $\tilde{u}_i(\vec{x},t_n)$ for every impeller phase, namely:

$$u_i'(\vec{x},t_n) = \tilde{u}_i(\vec{x},t_n) - \bar{u}_i(\vec{x}) \qquad (2)$$

Precisely, the deterministic fluctuation, or flow unsteadiness being observed in the absolute frame of reference, is a direct consequence of the tangential movement of the velocity gradients in the blade-to-blade passage. That is to say, it resembles how a time variation of the flow speed in the absolute frame is due to the circumferential displacement of an angular gradient in the relative

reference frame. Mathematically, it can be expressed as: $\frac{\partial}{\partial t} = -\Omega \frac{\partial}{\partial \theta}$. However, this is strictly valid only if the velocity in the relative frame is completely steady. This would be equivalent to admit that there are no interaction effects between the flow in the volute tongue and the velocity field within the impeller blades. Consequently, in order to handle the lack of uniformity of the real flow in what refers to the volute tongue interaction in the blade-to-blade patterns, an extra term to account for the pure interaction between both frames is considered in the analysis. This additional term, added to the periodic fluctuation of the deterministic excitations, is then expressed as:

$$u_i'(r,\theta,z,t) = u_i^{''(R)}(r,\theta - \Omega t, z) + \hat{u}_i(r,\theta,z,t) \tag{3}$$

In the previous equation, $\hat{u}_i(\vec{r}, t)$ stands for the pure unsteady term in the impeller flow-tongue interaction while $u_i^{''(R)}$ is the term to consider the difference between the time-averaged flow and the axisymmetric velocity component, $\tilde{u}_i^{(axi)}$, in the relative frame. This final component is retrieved through pitch-averaging (or circumferential averaging) and consists in the span-wise distribution of the velocity, which is no longer function of the relative frame to be considered, namely:

$$u_i^{''(R)}(r,\theta - \Omega t, z) = \bar{u}_i^{(R)}(r,\theta - \Omega t, z) - \tilde{u}_i^{(axi)}(r,z) \tag{4}$$

Operating with the procedure as explained, the time evolution of the impeller-volute interaction, $\hat{u}_i(\vec{r}, t)$, is found as the difference of the two terms that account for the impeller relative motion that is observed in the volute-tongue or absolute frame (eq. 3). To proceed correctly, a relocation routine of the variables has to be implemented to consider the change in the two frames according to: $\theta_{abs} = \theta_{rel} + \Omega t$. All the averaging procedures are graphically sketched in Fig. 5.

Fig. 5. Deterministic decomposition in both fixed and moving reference frames (adapted from Fernández Oro et al. [20]).

To sum up, the velocity field obtained by the URANS solution for a single volute centrifugal pump is split into a set of four components. The first one is the axisymmetric through-flow or pitch-averaged distribution of the velocity field. Following, there are the spatial blade-to-blade non-uniformities in the relative frame (R) and the volute-tongue gradients in the absolute frame (S). Those last ones are steady in their corresponding frames of reference because the time dependency has been dropped in the averaging procedures. Finally, it is found the pure temporal term, which is phase dependent and shows the impeller to volute-tongue flow interactions and is regarded as a totally non-linear term. Those four terms are included in the following decomposition:

$$\tilde{u}_i(\vec{x},t) = \underbrace{\tilde{u}_i^{(axi)}(r,z)}_{throughflow} + \underbrace{\hat{u}_i(r,\theta,z,t)}_{Temporal\ interaction} + \underbrace{u_i^{"(S)}(r,\theta,z) + u_i^{"(R)}(r,\theta - \Omega t,z)}_{Spatial\ non-uniformities} \qquad (5)$$

It must be noted that a similar decomposition can be attained using space-time periodicities. The deterministic velocity field can be expanded into a Fourier series with rotating circumferential modes representing the different interactions between the rotor and the stator (volute) flow, inspired in the Tyler and Sofrin rule; see Gerolymos et al. [25] or He [26]. Another possibility has been lately explored introducing modal decompositions – Trébinjac et al. [27] or Arnaud et al. [28] – to analyze unsteady flows within turbomachinery environments in order to save computational costs. In particular, Proper Orthogonal Decomposition (POD) can be also an interesting option to identify the relevant interaction mechanisms preserving most of the energy content of the velocity signals, but with a less number of modes; see Rochuon et al. [29] or Danaila et al. [30].

4.2. Deterministic stresses

As previously stated, the deterministic flow quantities are obtained after ensemble-averaging an unsteady signal in any turbomachinery environment. By definition, all the time scales correlate only with the periodic (deterministic) events associated to the rotation of the machine. In the case of a URANS simulation, and assuming that a convenient spectral gap exists, the temporal description of the flow guarantees that all the random fluctuations (turbulence) have been filtered out so the blade passing frequency and its harmonics are the only ones being preserved. Consequently, it can be obtained the deterministic stresses (according to the previous decomposition, Adamczyk, 1985), as those mixed products of the unsteady fluctuations departing from the time-averaged flow field. These stresses address the effects of unsteadiness caused by moving blade rows and are obtained according to:

$$\tau_{ij}^D = \frac{1}{T_B} \int_0^{T_B} [\tilde{u}_i(\vec{x}, t) - \bar{u}_i(\vec{x})] \cdot [\tilde{u}_j(\vec{x}, t) - \bar{u}_j(\vec{x})] dt \approx \frac{1}{N} \sum_{n=1}^N [\tilde{u}_i(\vec{x}, t_n) - \bar{u}_i(\vec{x})] \cdot$$
$$[\tilde{u}_j(\vec{x}, t_n) - \bar{u}_j(\vec{x})] \tag{6}$$

Where T_{BPF} corresponds to the blade passing period, sampled for a given discrete number N of intermediate instants (time steps per blade event), $\tilde{u}_i(\vec{x}, t_n)$ stands for the unsteady deterministic flow and $\bar{u}_i(\vec{x})$ represents the time-averaged velocity at every spatial position $\vec{x}$ inside the flow field, calculated according to (1).

Following, the deterministic kinetic energy (DKE) is calculated through the summation of the normal stresses in the main diagonal of the tensor, given by Meneveau et al. [31], as:

$$k^D = \frac{1}{2} \left(\tau_{rr}^D + \tau_{\theta\theta}^D + \tau_{zz}^D \right) \tag{7}$$

Where cylindrical coordinates have been employed because of the pump geometry. This metric of the energy associated to the deterministic unsteadiness can be easily compared to the turbulent kinetic energy, k^T, given by the turbulence model of the URANS simulation. As shown in section 4.1, the generation of the deterministic fluctuation, $u_i'(\vec{x}, t) = [\tilde{u}_i(\vec{x}, t) - \bar{u}_i(\vec{x})]$, can be further decomposed in new components, considering that spatial non-uniformities (gradients) in the relative frame of reference are sources of unsteadiness in the absolute frame, as derived by Leboeuf [32] and shown previously in eq. (2) to (5). Those spatial deviations $u_i^{"(R)}$ in the rotor from an axisymmetric flow produces unsteadiness in the stator and can be isolated introducing an additional circumferential averaging (pitch-averaging) along the angular extension of the impeller passage:

$$\tilde{u}_i^{(axi)}(r, z) = \frac{1}{\lambda}\int_{\theta_o}^{\theta_o + 2\pi/B} H\bar{u}_i(\vec{x})d\theta \approx \frac{1}{N_\theta}\sum_{n=1}^{N_\theta}\tilde{u}_i(\theta_n) \tag{8}$$

Where λ and H are functions to take into account the tangential thickness of the blades. Finally, this component is employed to retrieve a purely unsteady part that accounts for non-linear rotor-stator interactions:

$$\hat{u}_i(\vec{x}, t) = \tilde{u}_i(\vec{x}, t) - \tilde{u}_i^{(axi)}(r, z) - u_i^{"(R)}(\vec{x}) - u_i^{"(S)}(\vec{x}) \tag{9}$$

Where, for this last equation, $u_i^{"(S)}(\vec{x})$ stand for the spatial deviations from the axisymmetric flow in the absolute frame of reference. More details of this decomposition can be found in Leboeuf [32] and Fernández Oro et al. [20]. Because the deterministic fluctuation $u_i'(\vec{x}, t)$ is the combination of $u_i^{"(R)}(\vec{x})$ and $\hat{u}_i(\vec{x}, t)$ in the absolute frame of reference, $u_i'(\vec{x}, t) = \left[u_i^{"(R)}(\vec{x}) + \hat{u}_i(\vec{x}, t)\right]$, the deterministic correlation tensor for the stator flow can be rewritten as:

$$\overline{u_i'u_j'} = \overline{u_i''^{(R)}u_j''^{(R)}} + \overline{\hat{u}_iu_j''^{(R)}} + \overline{u_i''^{(R)}\hat{u}_j} + \overline{\hat{u}_i\hat{u}_j} \tag{10}$$

In this equation, the first term is the spatial correlation, the second and third terms are spatial-temporal mixed correlations and the forth term is a purely temporal correlation. The meaning and physical understanding of all these terms will be discussed in detail for a typical volute-type centrifugal pump in the following section.

5. Deterministic stresses inside the pump.

5.1. Unsteadiness and spectral gaps.

Deterministic stresses account for the effect of unsteadiness in the time-averaged flow caused by the moving blade rows. The periodic displacement of the blades generates an unsteady flow structure, as shown in Fig. 6-left, where the time evolution of the tangential velocity in the point C (located in front of the tongue, see sketch on the upper right corner) is plotted for the five flow rate conditions analysed. The velocity is normalized by the blade tip velocity and the traces have been repeated for convenience. At high flow rates (1.6 and $1.2\phi_N$), the impact of the unsteadiness is particularly intense, with velocity deficits, due to the blade wakes, as high as 40% and 20% of the through-flow velocity respectively. For nominal and lower flow rates, the effect of the wakes is found to be weaker, but still clearly retrieved from the numerical values. Regardless the flow rate, the influence of the unsteadiness is clearly prominent in the vicinity of the volute tongue, as shown in previous investigations by the authors, Barrio et al. [33].

Fig. 6. Temporal evolution of the tangential velocity at point C for different flow rate conditions (left plot) and corresponding spectra (right plot).

Fig.6-right also shows the corresponding spectra of those velocity signals where the BPF peak (189 Hz) and their harmonics are found. Obviously, due to the nature of the URANS modelling, contributions from other (non-deterministic) scales have been removed. However, the accurate employment of a URANS simulation requires the existence of a spectral gap between periodic (deterministic) unsteadiness and large-scale (random) turbulence in order to prevent unrealistic modelling issues. See Tucker [34] or Leschziner [35] for an excellent overview on the particular topic. In other words, the unsteady scales should range at lower frequencies than the beginning of the inertial subrange in the energy cascade, corresponding to the largest scales of the turbulent motion (i.e., $f_{ILS}/f_{BPF} > 1$). Table 2 provides a global estimation of those frequencies, obtained from the time-averaged values of the turbulent kinetic energy (TKE) within the interaction region in previous CFD simulations of the authors, Barrio et al. [33]. As given by the eddy-viscosity model of the numerical database, TKE is computed as the summation of the normal Reynolds stresses, that is, all the terms in the main diagonal of the Reynolds tensor. The size of the largest eddies has been assumed to be in the order of a fraction of the blade thickness for nominal conditions, or as a fraction of the impeller passage (outlet or inlet sections) for higher and lower flow rates, as suggested by the regions of turbulence generation observed in the contours of TKE close to the volute tongue (see Fig. 7 later).

Flow rate condition	TKE (m^2/s^2)	$u' = \sqrt{\dfrac{2}{3}TKE}$	L (mm)	f_{ILS} (Hz)	f_{ILS}/f_{BPF} (-)
$1.6\phi_N$	0.5	0.6	~1.75	330	1.74
$1.0\phi_N$	0.3	0.4	~0.9	497	2.63
$0.2\phi_N$	3	1.4	~4.5	314	1.66

Table 2. Estimation of integral scales of turbulence for different flow rate conditions. Comparison of deterministic and large-scale, turbulent phenomena.

As can be observed for all flow rates, the integral scales of turbulent motion are beyond the characteristic range of the fundamental frequency of the rotating blades, thus preserving the assumption of a spectral gap and providing correctness to the applicability of a URANS turbulence modelling in this case. The turbulent correlations, representing the modelled manifestation of the turbulent activity alone, is now presented for all the flow rates analysed in this investigation. Fig. 7 shows both instantaneous (top) and time-averaged (bottom) maps of TKE close to the volute tongue. For the instantaneous representation, only the snapshot corresponding to the position where the blade TE is facing the tongue is shown (this criterion will be repeated for unsteady variables throughout the whole paper). It can be observed how the generation of turbulence is mainly associated to the incoming flow onto the impeller inlet for higher flow rates, whereas highly turbulent regions are clearly shifted towards the pressure side of the blades TE for lower flow rates. Also, the position of the stagnation point in the tongue is severely displaced as a function of the operating flow rate (a well-known mechanism described in the open literature). Alternatively, the time-averaged maps show, in general, a quite axisymmetric behaviour, except for $0.2\phi_N$, where an important blade-tongue interaction is revealed when the next blade is arriving towards the tongue. To perform the average, a blade blockage factor must be introduced to consider the local angular thickness of the blades. Consequently, the blades are smeared out when averaged over the blade passing period.

Fig. 7. Distribution of TKE as a function of the flow rate: Instantaneous snapshot (top plot) and time-averaged distributions (bottom plot).

5.2. Deterministic stresses.

The deterministic stresses are evaluated from the difference between the unsteady (phase-averaged) flow and the time-averaged data, thus obtaining the squared product of the fluctuations,

as defined previously in Eq. 6. Moreover, the deterministic kinetic energy (DKE) is computed adding the normal stresses in the main diagonal of the deterministic tensor (Eq. 7). The computed distributions of DKE are presented in Fig. 8 for all the flow rate conditions (bottom plot) for comparison with the TKE results. Additionally, the instantaneous representation of the deterministic fluctuations for a single snapshot is also represented in the figure (top plot). Notice again how the time-averaged procedure removes the instantaneous presence of the blades.

Deterministic stresses appear as circumferential bands, mainly associated to the interior regions of the impeller that are continuously swept by the rotating blades (bottom plot). This is clear at nominal and high flow rates and represents the time-averaged distribution of the velocity fluctuations induced by the passing blades. As it will be discussed later, that typical pattern is provided by the main correlation of the deterministic stresses (see Eq. 10), the spatial correlation, which comprises the flow-turning effect (potential mechanism) of the blades. At lower flow rates, this contribution is partly masked by the influence of the temporal correlation that takes into account the blade-tongue interaction in the time-averaged flow structure: although the characteristic circumferential bands are quite preserved, a region of high values close to the volute tongue is predominant. Also note that both deterministic and turbulent stresses present similar values and overall trends with the flow rate, with lower values at nominal than at off-design conditions.

Fig. 8. Distribution of DKE as a function of the flow rate: Instantaneous snapshot of the deterministic fluctuations (top plot) and distributions (bottom plot).

As can be observed at the top plot in Fig. 8, instantaneous fields of deterministic fluctuations resemble a quite local behaviour and seem to be linked to the blade sides in the relative frame (within the impeller), thus leading to the generation of circumferential bands when averaged in the absolute frame (are rotated). This is not the case for $0.2\phi_N$ where the blade-tongue

interaction, due to the massive flow separation, induces highly unsteady, viscous mechanisms. The deterministic shear stress for the radial-tangential (in-plane) component also shows a typical band-like pattern and has not been included for brevity.

Therefore, and due to this axisymmetric feature of the deterministic stresses, it is quite useful to represent all these distributions in Fig. 8 after an additional pitch-averaging (or circumferential averaging). It is interesting to observe the radial evolution of the stress as we move through the impeller, which also provides the description of the stresses for 1-D through-flow models. For completeness, both pitch-averaged distribution of turbulence and deterministic unsteadiness are included in Fig. 9. For nominal and high flow rates, the turbulence kinetic energy is quite reduced and decreasing along the impeller passage (see Fig. 9, left). For $1.6\phi_N$ and $1.2\phi_N$ is later increased because of the separation region in the volute discharge conduit, well downstream of the impeller. For lower flow rates, turbulence exhibits an inverted behaviour, being progressively increased along the passages, with high maximum values at the blades TE. Afterwards, the levels decay severely with large rates of turbulent dissipation in the volute casing.

Conversely, deterministic distributions (Fig. 9, right) present quite similar evolutions for all the flow rates, with maximum values in the first half of the impeller passages, followed by an abrupt reduction towards the impeller exit and, finally, a sharp peak at the impeller outlet. Surprisingly, the nominal flow rate is not the case showing the lowest values of deterministic fluctuations, being the lowest flow rate the condition with the lowest unsteadiness. Note also how the volute tongue is completely absent of deterministic contributions. For this centrifugal pump, deterministic unsteadiness is exclusively confined to the impeller region, where the passage flow and the wake-jet pattern at the impeller outlet are influenced by the non-uniformities associated to the stagnation conditions of the volute tongue.

Fig. 9. Pitch-averaged distributions of turbulent (left) and deterministic (right) stresses as a function of the flow rate.

Additionally, the deterministic sources can be considered as an alternative metric to characterize some secondary flows due to the superimposition of relative flow patterns within the volute flow. The internal displacement flow in the impeller passages, concentrating the flow towards the suction side; the classic jet-wake pattern or the development of recirculation vortex and separation in the blades TE are typical phenomena found in single volute centrifugal pumps (Barrio et al. [33]). To analyse them, the Rossby number is usually introduced in the scientific literature (see Moore et al. [36]; Moore and Moore [37] or Lakshmnirayana and Horlock [38]) in order to assess the effect of the curvature in the impeller passages and the rotation on the stability (here viewed as unsteadiness) of the flow. The classic definition by Moore, relating the relative velocity W through the passages, with the rotation and the local curvature of the streamlines imposed by the blades camber has been employed here: $Ro = W/\Omega r_n$. High Ro numbers are associated to high relative velocities and large curvatures (small local blade radii), while small Ro numbers are found in case of low flowrates and mild bending. Moreover, classic references indicate that large Ro are associated to stable wake flow close to the shroud wall while low Ro lead to stable flow in the suction side of the blades.

Fig. 10-top shows the circumferential distribution of the Rossby number in the impeller passages for the different flow rates analysed. It is confirmed that higher flow rates experience large values of Ro in the inlet zone of the impeller, especially close to the suction side. In the case of lower flow rates, a recirculation vortex induces high relative velocity values towards the blade TE which is facing the volute tongue, promoting a thin region with large Ro values.

Fig. 10. Distributions of the Rossby number in the impeller passages as a function of the flowrate (top). Correlations between pitch-averaged distributions of DKE and Rossby number for different flow rates (bottom).

To give more insight, the pitch-averaged distributions of the Rossby number and the Deterministic Kinetic Energy are compared in Fig. 10-bottom. It is noticeable that a significant correlation is established in the results for all the flow rates observed, thus confirming that deterministic unsteadiness may be perceived as sources of secondary flows. In particular, next section, which involves a further decomposition of the deterministic stresses into spatial and temporal components, reveals that the spatial correlation, associated to the circumferential motion of the rotor gradients is responsible for the internal displacement flow and the stability of the wake-flow pattern; whereas the pure temporal term is specifically linked to a vortex recirculation established close to the volute tongue (at the lowest flowrate). If this impeller-tongue interaction is to be limited, then it is necessary to optimize the blade profiling close to the TE or modify the impeller-tongue distance to reduce the vortex.

5.3. Impact of the different Correlations on the Deterministic Stresses.

Following, the relevance of the spatial, temporal and spatial-temporal correlations that compose the deterministic stresses is shown in this final subsection. Firstly, the effect of the pure-unsteady interaction of the temporal correlation is shown in Fig. 11. The time-averaged maps reveal the existence of a region close to the tongue where high temporal (periodic) interaction between viscous and potential effects arises. At $1.6\phi_N$, this region is perfectly aligned with the angular location of the tongue, limited to a small region at the impeller outlet. At $1.2\phi_N$ and $1.0\phi_N$ this contribution is really marginal, but it is again predominant for lower flow rates at $0.6\phi_N$ and $0.2\phi_N$. The tangential extension of this hot spot is practically equivalent to the width of the impeller passage at the outlet and it is extended radially along ¼ of the blade chord. This source of

unsteadiness is clearly associated to the periodic interaction of the separated flow in the pressure side of the blades with the geometrical blockage imposed by the tongue.

Fig. 11. Distribution of the temporal correlation of the DKE as a function of the flow rate.

Fig. 12 presents the results of the mixed spatial-temporal correlation as a function of the flow rate. It is important to see that the spatial-temporal correlation might be negative or positive, pending on the direction of the fluctuations of both crossed velocities involved. This leads to a strong impact on the circumferential non-uniformities of the global deterministic stresses. Also, it has to be considered two times according to eq. 10. The results show that the order of magnitude of the correlation is quite similar for all the flow rates analysed, with a characteristic range between -0.75 and 0.75 approximately. For higher flow rates, the influence of the spatial non-uniformities is more evident, with the fingerprint of the typical circumferential bands. For lower flow rates, the impact of the temporal non-uniformities is dominant, with positive values before the tongue and negative ones afterwards.

Fig. 12. Distribution of the spatial-temporal correlation of the DKE as a function of the flow rate.

To better clarify the idea, Fig. 13 represents the pitch-averaged distribution of the spatial correlation for different flow rates. In addition, the maps (before tangentially-averaged) corresponding to the highest and lowest flow rates are also introduced for traceability. The axisymmetric pattern of the spatial correlation justifies the use of a single plot to represent its radial evolution for the meridional planes under study. The evolution of this correlation with the flow rate is equivalent to the one previously discussed in Fig. 9 for the global deterministic stresses. It can be observed that the values are even slightly higher than those of the global results in Fig. 9-right because of the effect of the negative values introduced by the mixed spatial-temporal

correlation. In the case of the nominal flow rate, the value is practically uniform within the impeller passage, only peaked at the blade TE.

Fig. 13. Distribution of the pitch-averaged spatial correlation of the DKE as a function of the flow rate.

To conclude the analysis of the results, the comparison of the different products of velocity fluctuations concerning deterministic (with all the correlations) and turbulent fluctuations are summarized in Fig. 14. Only the first time step for the highest, nominal and lowest flow rates is shown in the representation for brevity. The instantaneous products can be even interpreted as noise sources according to different aero-acoustic analogies, whose origin can be related to deterministic interactions or turbulent broadband instabilities. For the highest flow rate, spatial deterministic stresses are dominant in the impeller region, mainly associated to the suction side of the blades, while turbulent generation is weaker and restricted to the entrance of the impeller passages. In the case of the nominal flow rate, deterministic sources present a similar pattern, introducing relevant unsteadiness once the blades have passed by. Turbulent kinetic energy is spread through the passages, with moderate turbulent regions in the outer half of the blades pressure side and also in the blades TE. However, at the lowest flow rate, the temporal correlation of the deterministic stresses plays a major role, contributing to address the fluctuations of the detached flow in the pressure side of the blades. More precisely, the circumferential displacement of the massive separation in the blades is the flow feature captured by the spatial correlation. It can be observed how the turbulent stresses resemble those characteristics and exhibit also relevant values in the pressure side of the blades. In this case, the turbulent mechanisms are shed with a certain angular delay with respect the deterministic stresses.

Fig. 14. Comparison of instantaneous fluctuations related to deterministic (identifying correlations) and turbulent mechanisms as a function of the flow rate: highest (top), nominal (middle) and lowest (bottom) flow conditions.

6. Conclusions.

An existing and validated 3D URANS numerical model has been revisited in this paper to perform a detailed deterministic analysis of the unsteady flow structures. This methodology, oriented towards a post-processing tool, allows to identify the origin and nature of the relevant unsteady sources that play a major role in the performance of the turbomachine. A better understanding of the unsteadiness, the transport of turbulent scales and the mechanisms responsible for impeller-volute interactions is essential to foresee a possible geometrical optimization, becoming an important objective at the current technological status.

First of all, overall trends in the evolution of deterministic and turbulent fluctuations in terms of kinetic energy were analysed for different flow rate conditions. Turbulent structures are important for higher and lower flow rates only, associated to flow separations in the blades TE, and persist in the vicinity of the volute tongue. Deterministic stresses are predominant in both LE and TE of the blades for all flow rate conditions and they are completely absent in the volute tongue. Globally speaking, both turbulent and deterministic scales present similar intensities although deterministic contributions are higher within the impeller of the pump. In addition, all these variables show lower values at nominal flow rates and increasing ones for off-design conditions, resembling the classical V-shaped curves that were obtained several decades ago for the forces in the shaft of similar geometries.

The further decomposition of the deterministic stresses into spatial and temporal correlations has provided also valuable information. The pure unsteady component (temporal correlation) has revealed the significant interaction established between the detached flow in the pressure side of the blades and the tongue blockage for low flow rates. On the contrary, wake-tongue interactions are practically negligible, thus confirming that the tongue promotes a significant interference on the impeller flow structures, but the impeller wakes have no effect over the flow structures of the volute tongue.

Additionally, the study of the mixed spatial-temporal correlation has shown that, for the nominal flow rate, the value is practically uniform within the impeller passage, only peaked at the blade TE. Clear deviation from this trend is observed for both high and low flow rates. A full range of behaviours have been studied in order to search for a full definition of the existing interactions.

Finally, a comparison of the different products of velocity fluctuations concerning deterministic and turbulent fluctuations was considered. For the nominal flow rate, turbulent kinetic energy is spread through the passages, with moderate turbulent regions in the outer half of the blades pressure side and also in the blades. At off-design conditions, the turbulent mechanisms are shed promoting an angular delay with respect the deterministic stresses.

Therefore, for the flow in the pump, substantial differences have been observed as a function of the flow rate or working condition. Blade optimization could target both the blade leading and trailing edges. For the first one, similar evolutions for all the flow rates regarding the deterministic stresses, with maximum values in the first half of the impeller passages was found. The latter position shows a growing peak in the pitch-averaged spatial distribution of the turbulent kinetic energy.

Nomenclature.

b	=	Impeller width, [m].
B	=	Number of blades, [–].
BPF	=	Blade Passing Frequency.
CFD	=	Computational Fluid Dynamics.
D	=	Impeller diameter, [m].
DKE	=	Deterministic Kinetic Energy.
f	=	Frequency, $[s^{-1}]$.

H	=	Head; Blockage function.
ILS	=	Integral Length Scale.
L	=	Integral length scale, [m].
LE	=	Blade Leading Edge.
k^D	=	Deterministic kinetic energy, $[m^2/s^2]$.
k^T	=	Turbulent kinetic energy, $[m^2/s^2]$.
K	=	Valve loss coefficient, $[m/(m^3/s)^2]$.
n_s	=	Specific speed, $[–]$.
n	=	Single realization.
N	=	Number of time steps per blade event.
POD	=	Proper Orthogonal Decomposition.
Q	=	Volumetric flowrate, $[m^3/s]$.
r	=	Radial coordinate, [m].
r_n	=	Radius of curvature, [m]
RNG	=	Renormalization Group (k-epsilon model).
Ro	=	Rossby number, [-]
SMM	=	Sliding Mesh Model.
t	=	Time, [s].
T_B	=	Blade passing period, [s].
TE	=	Blade Trailing Edge.
URANS	=	Unsteady Reynolds-Averaged Navier-Stokes.
$\tilde{u}$	=	Ensemble-averaged (U-RANS) velocity, [m/s].
$\bar{u}$	=	Time-averaged velocity, [m/s].
$\hat{u}$	=	Unsteady impeller-volute fluctuation, [m/s].
u'	=	Deterministic velocity fluctuation, [m/s].
u''	=	Spatial velocity fluctuation, [m/s].

U_b	=	Blade peripheral velocity, [m/s].
W	=	Relative velocity, [m/s].
$\vec{x}$	=	Position vector.
z	=	Axial coordinate, [m].

Greek Letters

β	=	Blade angle, [deg].
θ	=	Angular coordinate, [rad].
λ	=	Angular blade thickness, [deg].
ϕ	=	Flow coefficient, [–].
ρ	=	Density, [kg/m^3].
τ^D	=	Deterministic stress, [m^2/s^2].
Ω	=	Rotational speed, [rad/s].

Superscripts and Subscripts

‾	=	Time-averaging.
~	=	Ensemble-averaging.
(axi)	=	Pitch-averaging.
abs	=	Absolute reference frame.
b	=	Blade
i,j,k	=	Radial, circumferential and axial components.
N	=	Nominal conditions.
(R)	=	Rotor frame of reference (relative).
rd	=	Radial component.
rel	=	Relative reference frame.
(S)	=	Stator frame of reference (absolute).

| tg	=	Tangential component.
1,2	=	Impeller inlet, outlet.

Acknowledgements.

References.

[1] Binder, R.C., Lafayette, IND., Knapp, R.T., 1936, "Experimental determination of the flow characteristics in the volutes of centrifugal pumps," Transactions of the ASME. Hyd., 58-4, pp. 649−663.

[2] Bowerman, R.D., Acosta A.J., 1957, "Effect of the volute on performance of a centrifugal pump impeller," Transactions of the ASME, 79, pp. 1057−1069.

[3] Adkins, D.R., Brennen, C.E., 1988, "Analysis of hydrodynamic radial forces on centrifugal pump impellers," ASME J Fluid. Eng., 110, pp. 20−28.

[4] Miner, S.M., Flack, R.D., Allaire, P.E., 1992, "Two dimensional flow analysis of a laboratory centrifugal pump," ASME J Fluid. Eng., 114, pp. 333−339.

[5] Greitzer, E.M., 1981, "The stability of pumping systems – The 1980 Freeman Scholar Lecture," ASME J Fluid. Eng., 103, pp. 193−242.

[6] Lakshminarayana, B., 1991, "An assessment of computational fluid dynamic techniques in the analysis and design of Turbomachinery – The 1990 Freeman Scholar Lecture," ASME J Fluid. Eng., 113, pp. 315−352.

[7] Brennen, C.E., 1994, Hydrodynamics of Pumps, Oxford University Press and Concepts ETI Inc.

[8] Tsukamoto, H., Uno, M., Hamafuku, H., and Okamura, T., 1995, "Pressure Fluctuation Downstream of a Diffuser Pump Impeller," The Second Joint ASME/JSME Fluids Engineering Conference, Forum of Unsteady Flow, ASME, New York, FED−Vol. 216, pp. 133−138.

[9] Kaupert, K.A., Staubli, T., 1999, "The unsteady pressure field in a high specific speed centrifugal pump impeller. Part I: Influence of the volute," ASME J Fluid. Eng., 121, pp. 621−626.

[10] Dong, R., Chu, S., Katz, J., 1997, "Effect of modification to tongue and impeller geometry on unsteady flow, pressure fluctuations and noise in a centrifugal pump," ASME J Turbomach., 119, pp. 506−515.

[11] Wuibaut, G., Bois, G., Dupont, P., Caignaert, G., Stanilas, M., 2002, "PIV Measurements in the impeller and vaneless diffuser of a radial flow pump in design and off-design operating conditions," ASME J Fluid. Eng., 124, pp. 791−797.

[12] Croba, D., Kueny, J.L., 1996, "Numerical calculation of 2D, unsteady flow in centrifugal pumps: impeller and volute interaction," Int J Numer. Methods in Fluids, 22, pp. 467−481.

[13] Shi, F., Tsukamoto, H., 2001, "Numerical study of pressure fluctuations caused by impeller-diffuser interaction in a diffuser pump stage," ASME J Fluid. Eng., 123, pp. 466–474.

[14] Goto, A., Zangeneh, M., 2002, "Hydrodynamic design of pump diffuser using inverse design method and CFD," ASME J Fluid. Eng., 124, pp. 319-328.

[15] González, J., Fernández, J., Blanco, E., Santolaria, C., 2002, "Numerical simulation of the dynamic effects due to impeller-volute interaction in a centrifugal pump,". ASME J Fluid. Eng., 124, pp. 348–355.

[16] Wu, D., Yan, P., Chen, X., Wu, P., Yang, S., 2015, "Effect of trailing-edge modification of a mixed-flow pump," ASME J Fluid. Eng., 137, paper 101205, pp. 1-9.

[17] Adamczyk, J.J., 1985, "Model equation for simulating flows in multistage turbomachinery,". ASME Paper No. 85-GT-226.

[18] Adamczyk, J.J., 2000, "Aerodynamic analysis of multistage turbomachinery flows in support of aerodynamic design," ASME J Turbomach., 122, pp. 189–217.

[19] Van Zante, D.E., Adamczyk, J.J., Strazisar, A.J., Okiishi, T.H., 2002, "Wake recovery performance benefit in a high-speed axial flow compressor," ASME J Turbomach., 124, pp. 275–284.

[20] Fernández Oro, J.M., González, J., Argüelles, K.M., Guerras, F.I., 2011, "Decomposition of deterministic unsteadiness in a centrifugal turbomachine: non-linear interactions between the impeller flow and volute for a double suction pump," ASME J Fluid. Eng., 133, paper 011103, pp. 1–10.

[21] González, J., Parrondo, J., Santolaria, C., Blanco, E., 2006. "Steady and unsteady radial forces for a centrifugal pump with impeller to tongue gap variation," ASME J Fluid. Eng., 128, pp. 454–462.

[22] Parrondo, J.L., González, J., Fernández, J., 2002, "The effect of the operating point on the pressure fluctuations at the blade passage frequency in the volute of a centrifugal pump," ASME J Fluid. Eng., 124, pp. 784–790.

[23] González, J., Santolaria, C., 2006, "Unsteady flow structure and global variables in a centrifugal pump," ASME J Fluid. Eng., 128, pp. 937−946.

[24] Barrio, R., Blanco, E., Parrondo, J., González J., Fernández, J., 2008, "The effect of impeller cutback on the fluid-dynamic pulsations and load at the blade-passing frequency in a centrifugal pump," ASME J Fluid. Eng., 130, paper 111102, pp. 1−11.

[25] Gerolymos GA, Michon GJ, Neubauer J., 2002, "Analysis and application of chorochronic periodicity in turbomachinery rotor/stator interaction computations," J Propulsion and Power, 18(6), pp. 25−39.

[26] He L., 2010, "Fourier methods for turbomachinery applications," Prog. in Aerospace Sciences, 46, pp. 329-341.

[27] Trébinjac I, Charbonnier D, Leboeuf F., 2005, "Unsteady rotor-stator interaction in high speed compressor and turbine stages," J Thermal Science, 14(4), pp. 289−297.

[28] Arnaud D, Ottavy X, Vouillarmet A., 2004, "Experimental investigation of the rotor-stator interactions within a high-speed, multi-stage, axial compressor. Part 2 – Modal analysis of the interactions," ASME Paper No. GT2004−53778, Vienna (Austria), 14−17 June.

[29] Rouchon, N.; Trébinjac, I.; Billonnet, G., 2006, "An Extraction of the Dominant Rotor-Stator Interaction Modes by the Use of Proper Orthogonal Decomposition (POD)," J Thermal Science, 15(2), pp. 109−114.

[30] Danaila, S.; Niculescu, M.L., 2010, "Proper Orthogonal Decomposition Analysis for Unsteady Rotor-Stator Interaction in a Low Pressure Centrifugal Compressor," WSEAS Transactions of Fluid Mechanics, 5(3), pp. 226−235.

[31] Meneveau, C., Katz, J., 2002, "A Deterministic Stress Model for Rotor-Stator Interactions in Simulations of Average-Passage Flow," ASME J Fluid. Eng., 124, pp. 550−554.

[32] Leboeuf, F., 2002, "Unsteady Flow Analysis in Transonic Turbine and Compressor Stages," VKI Lecture Series "Recent Developments in Numerical Methods for Turbomachinery Flows", 2002−01.

[33] Barrio, R., Parrondo, J., Blanco, E., 2010, "Numerical Analysis of the Unsteady Flow in the Near-Tongue Region in a Volute-Type Centrifugal Pump for different Operating Conditions," Computers & Fluids, 39, pp. 859−870.

[34] Tucker, P.G., 2011, Unsteady Computational Fluid Dynamics in Aeronautics, Springer, Berlin.

[35] Leschziner, M., 2016, Statistical Turbulence Modelling for Fluid Dynamics – Demystified, Imperial College Press, London.

[36] Moore, J., Moore, J.G., Johnson, M.W., 1977, "On Three-Dimensional Flow in Centrifugal Impellers," Cambridge Univ. Eng. Dept. Rep. Turbo/TR 85 also Aeronautical Research Council CP No. 1384.

[37] Moore, J., Moore, J.G., 1981, "Calculations of Three-Dimensional, Viscous Flow and Wake Development in a Centrifugal Impeller," ASME J. Eng. for Power, 103, pp. 367−372.

[38] Lakshminarayana, B., Horlock, J. H., 1973, "Generalised Expressions for Secondary Vorticity using Intrinsic Coordinates". J of Fluid Mech., 59, pp. 97−115.
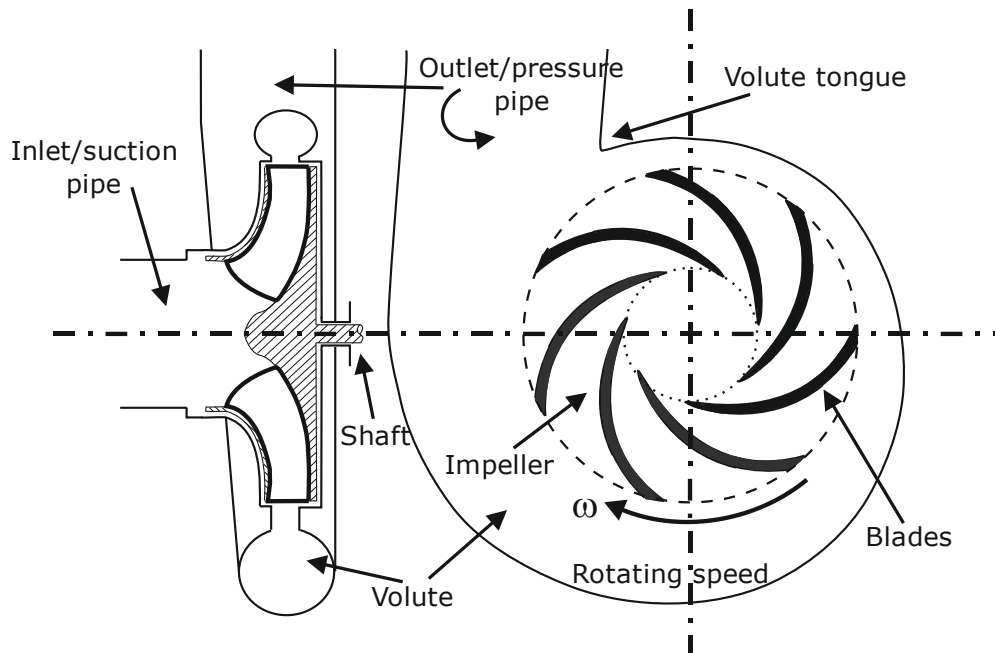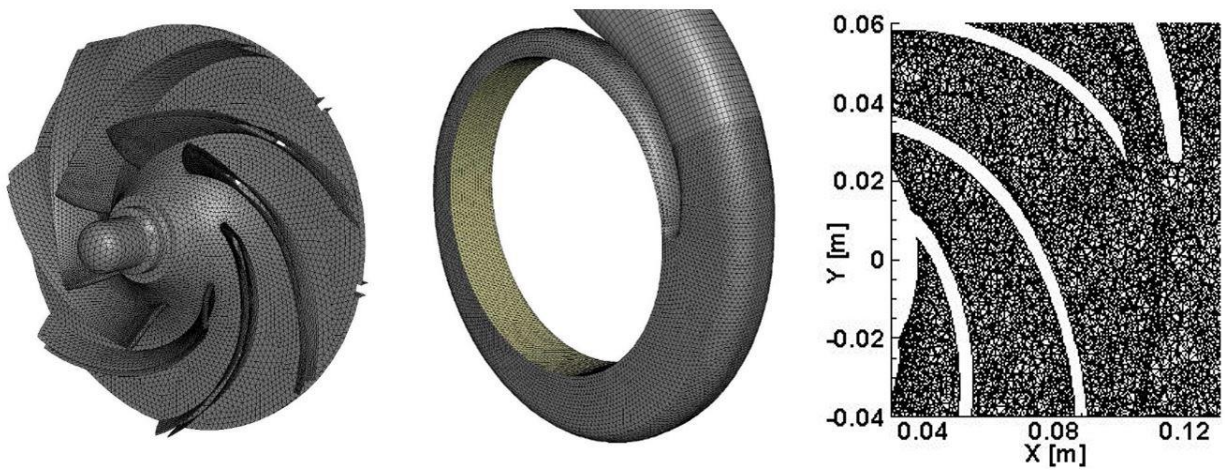
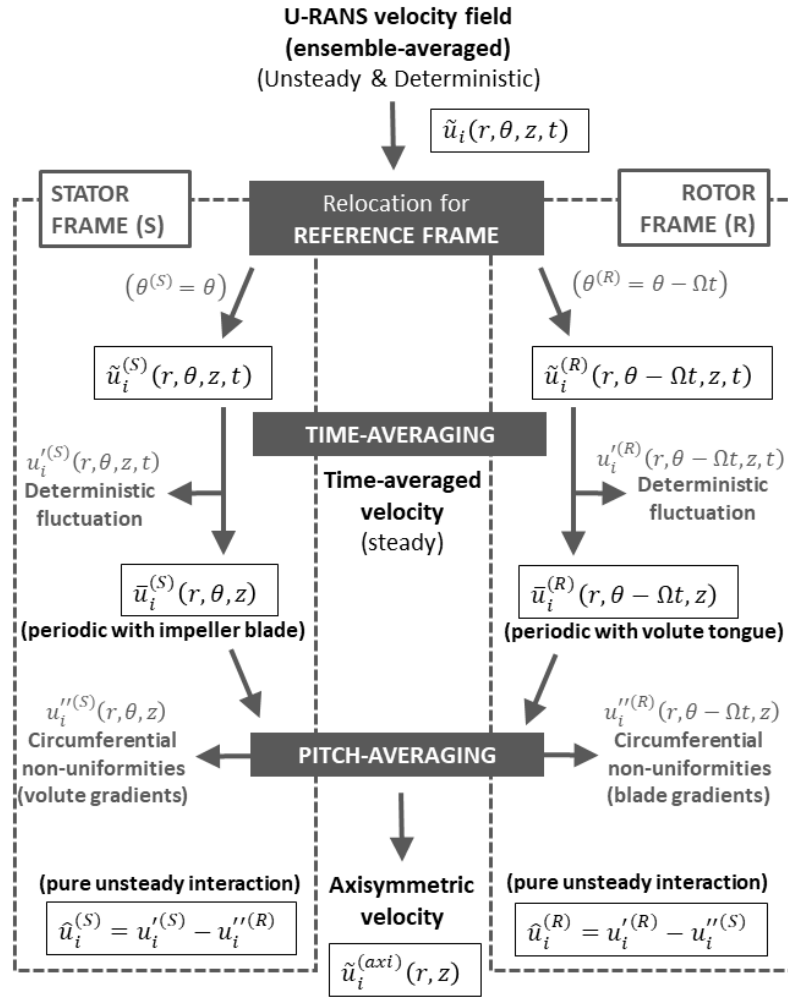**Fig. 1. Global sketch of a typical centrifugal pump.**

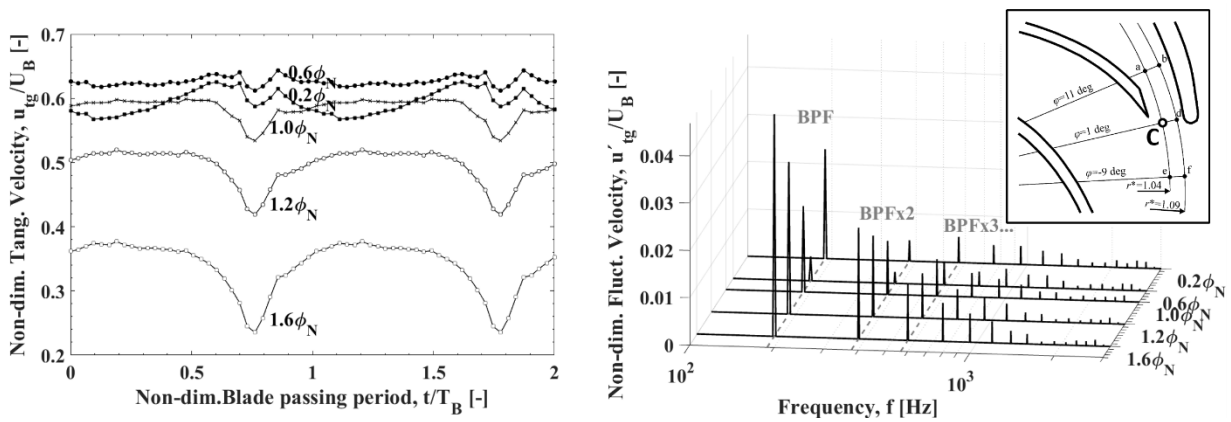**Fig. 2. Single volute commercial pump used for the present study.**
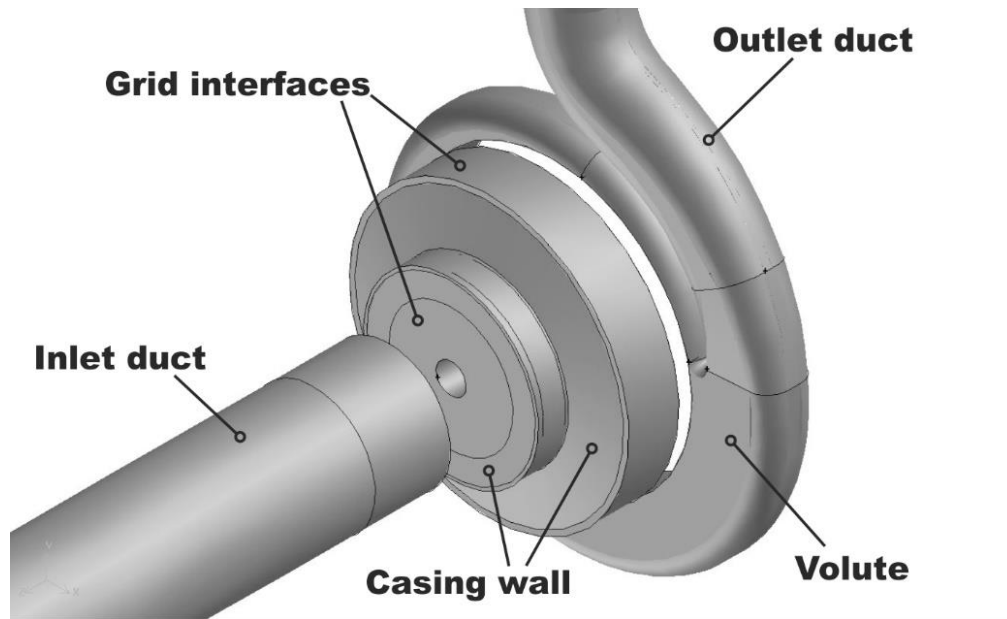
Fig. 3. General view of the numerical model.

Fig. 4. Details of the surface mesh of the impeller (left) and volute (center). Transversal cut of the 3D mesh in the vicinity of the volute tongue (right).
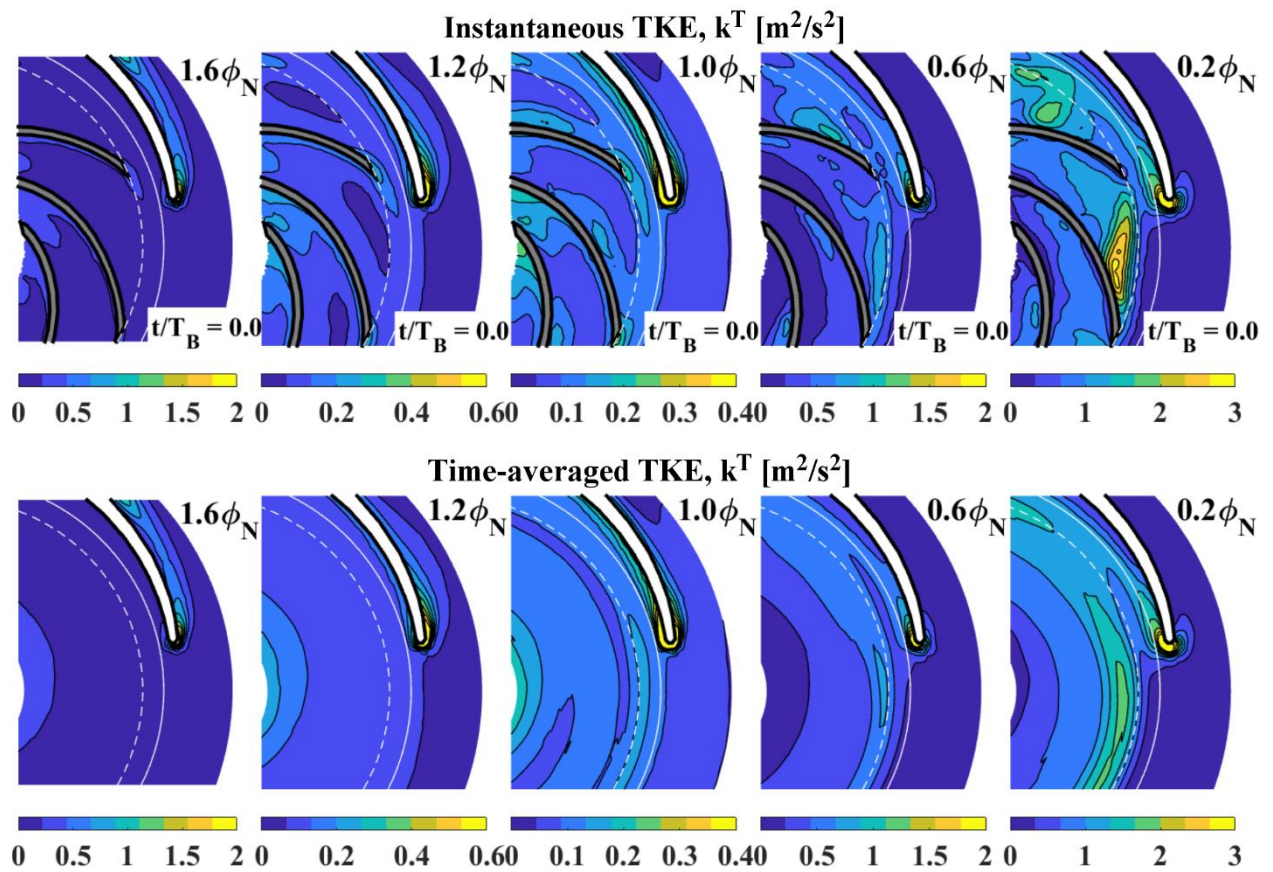
U-RANS velocity field
(ensemble-averaged)
(Unsteady & Deterministic)

$$\tilde{u}_i(r,\theta,z,t)$$

STATOR FRAME (S)

Relocation for REFERENCE FRAME

ROTOR FRAME (R)

$$\left(\theta^{(S)} = \theta\right)$$

$$\left(\theta^{(R)} = \theta - \Omega t\right)$$

$$\tilde{u}_i^{(S)}(r,\theta,z,t)$$

$$\tilde{u}_i^{(R)}(r,\theta - \Omega t,z,t)$$

TIME-AVERAGING

Time-averaged velocity (steady)

$$u_i'^{(S)}(r,\theta,z,t)$$
Deterministic fluctuation

$$u_i'^{(R)}(r,\theta - \Omega t,z,t)$$
Deterministic fluctuation

$$\bar{u}_i^{(S)}(r,\theta,z)$$

(periodic with impeller blade)

$$\bar{u}_i^{(R)}(r,\theta - \Omega t,z)$$

(periodic with volute tongue)

$$u_i''^{(S)}(r,\theta,z)$$
Circumferential non-uniformities (volute gradients)

PITCH-AVERAGING

$$u_i''^{(R)}(r,\theta - \Omega t,z)$$
Circumferential non-uniformities (blade gradients)

(pure unsteady interaction)

$$\hat{u}_i^{(S)} = u_i'^{(S)} - u_i''^{(R)}$$

Axisymmetric velocity

$$\tilde{u}_i^{(axi)}(r,z)$$

(pure unsteady interaction)

$$\hat{u}_i^{(R)} = u_i'^{(R)} - u_i''^{(S)}$$

Fig. 5. Deterministic decomposition in both fixed and moving reference frames (adapted from Fernández Oro et al. [20]).
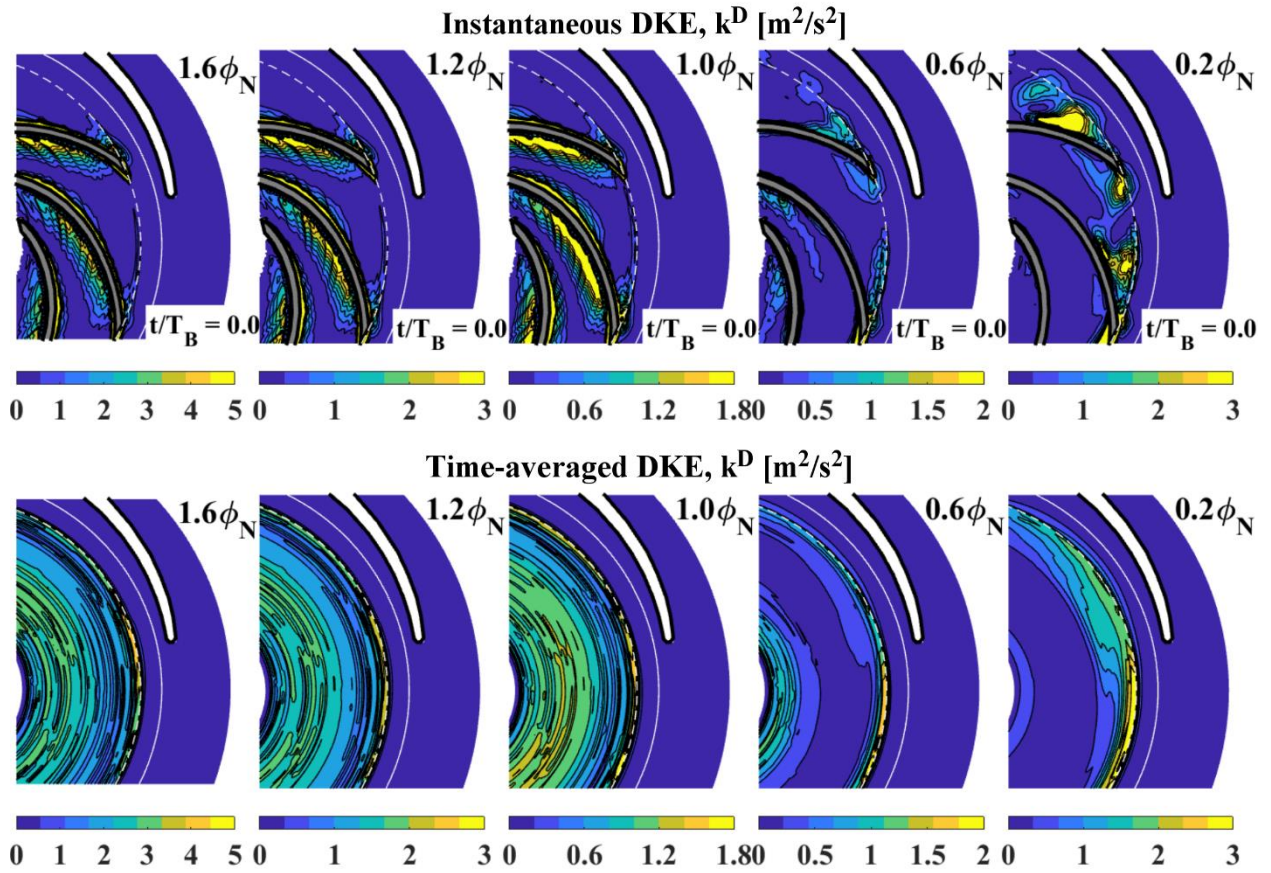

Fig. 6. Temporal evolution of the tangential velocity at point C for different flow rate conditions (left plot) and corresponding spectra (right plot).
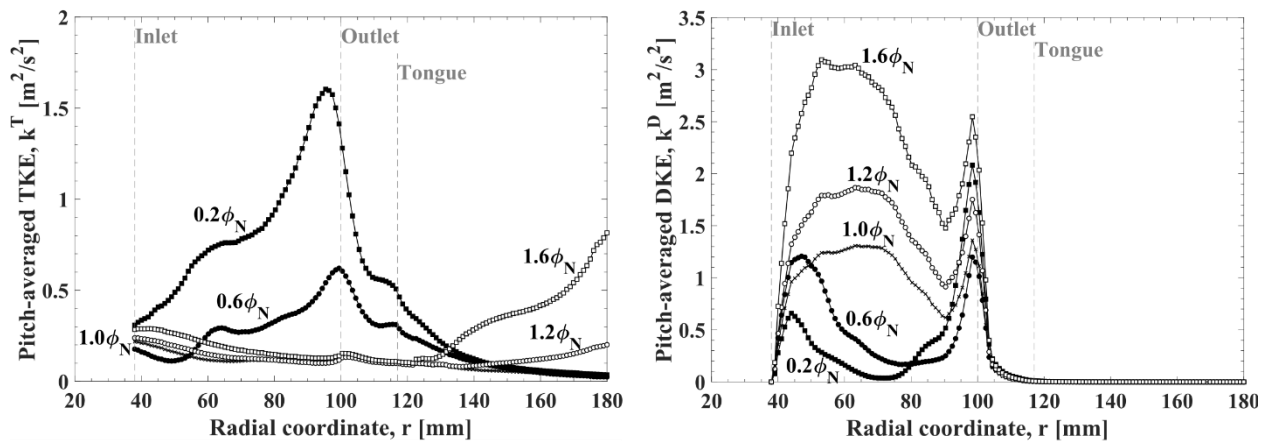
32

Fig. 7. Distribution of TKE as a function of the flow rate: Instantaneous snapshot (top plot) and time-averaged distributions (bottom plot).

Instantaneous DKE, k^D [m²/s²]

Time-averaged DKE, k^D [m²/s²]

Fig. 8. Distribution of DKE as a function of the flow rate: Instantaneous snapshot of the deterministic fluctuations (top plot) and distributions (bottom plot).

Fig. 9. Pitch-averaged distributions of turbulent (left) and deterministic (right) stresses as a function of the flow rate.

Rossby Number, Ro=W/Ωr$_n$ [-]

Pitch-averaged DKE, k^D /U$_b$V$_{rd}$[-] vs. Pitch-averaged Ro [-]

Fig. 10. Distributions of the Rossby number in the impeller passages as a function of the flowrate (top). Correlations between pitch-averaged distributions of DKE and Rossby number for different flow rates (bottom).
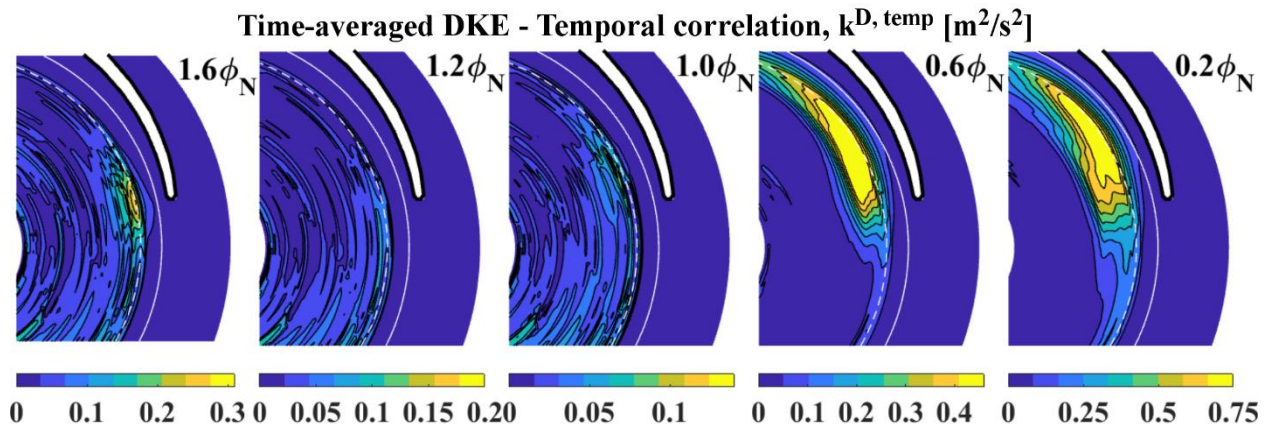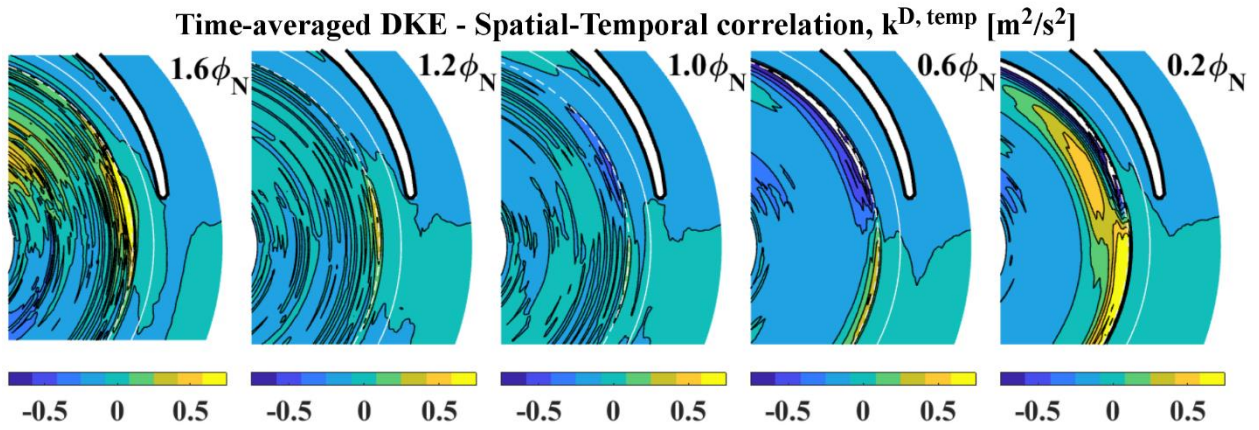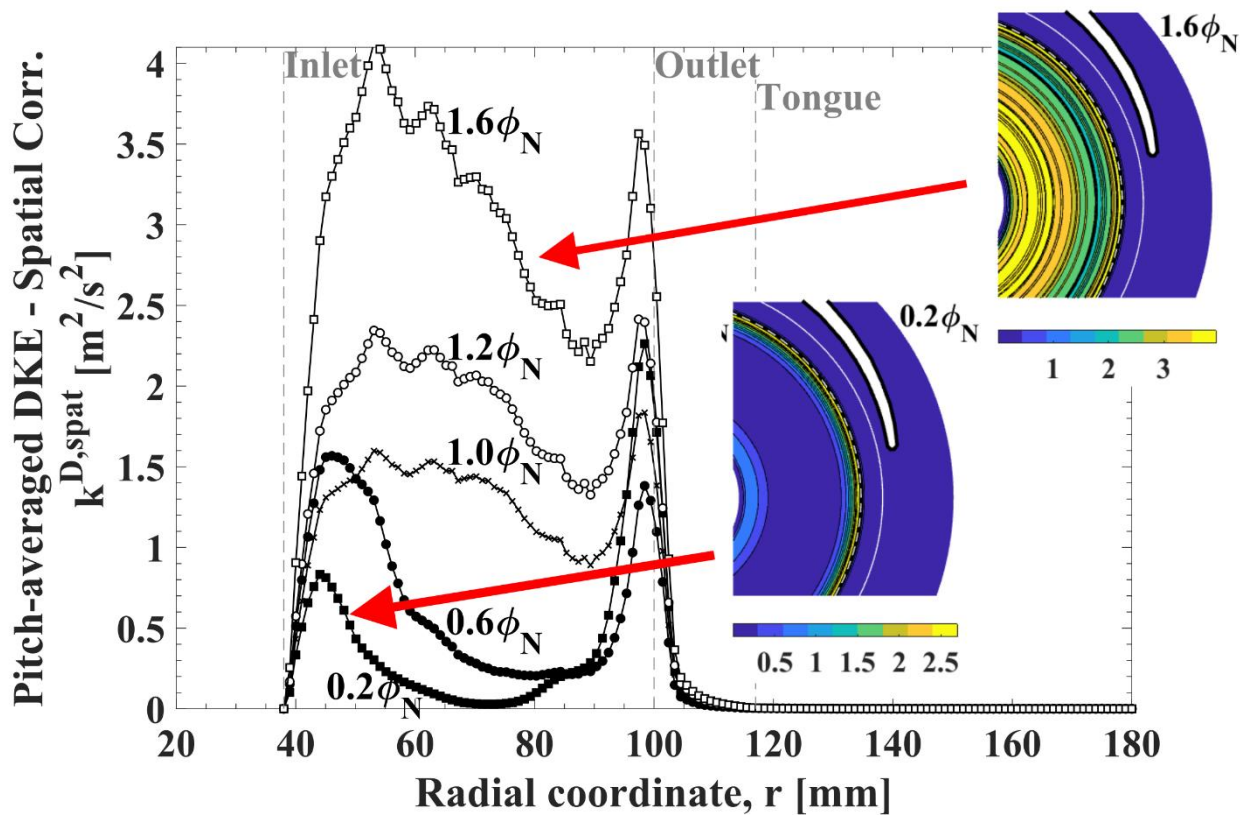
Time-averaged DKE - Temporal correlation, k$^{D, temp}$ [m^2/s^2]
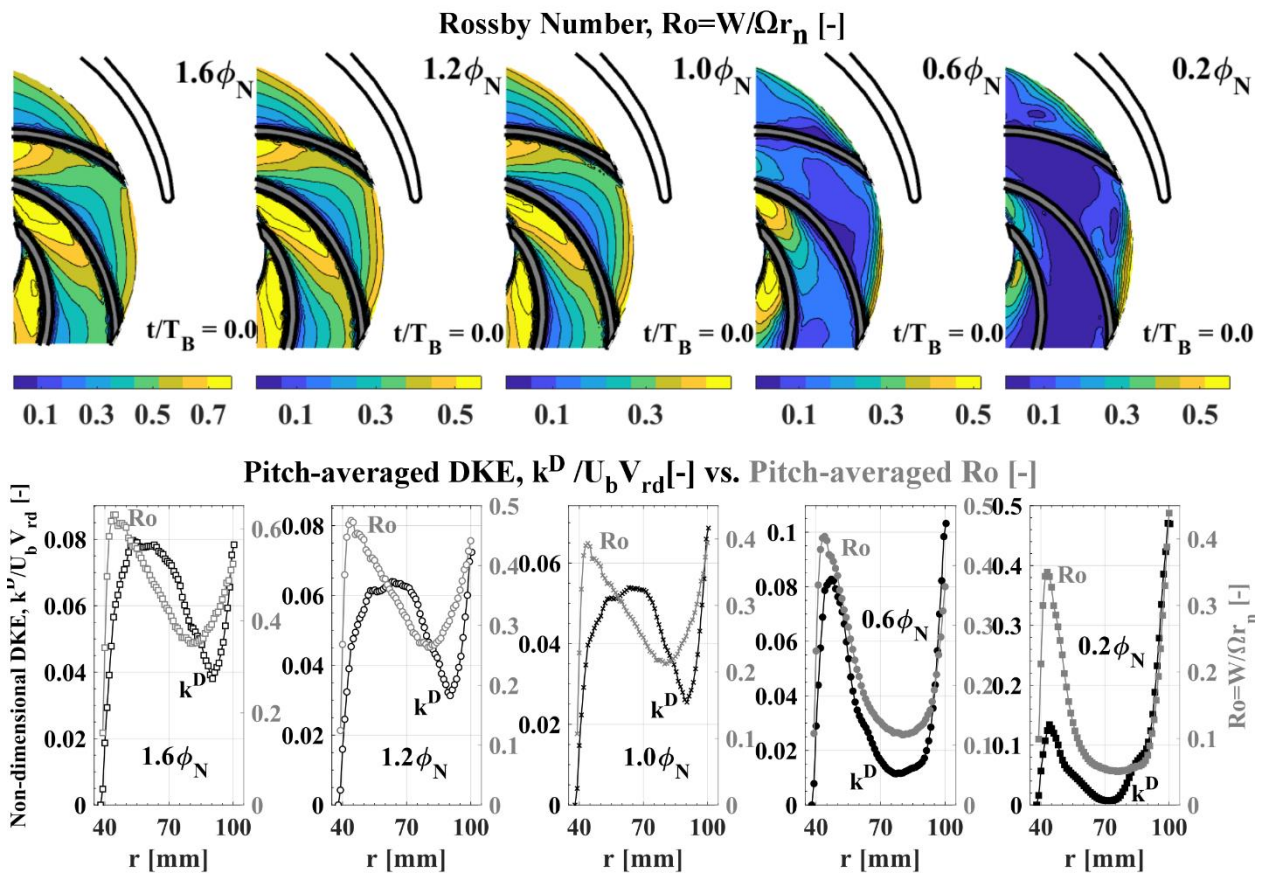
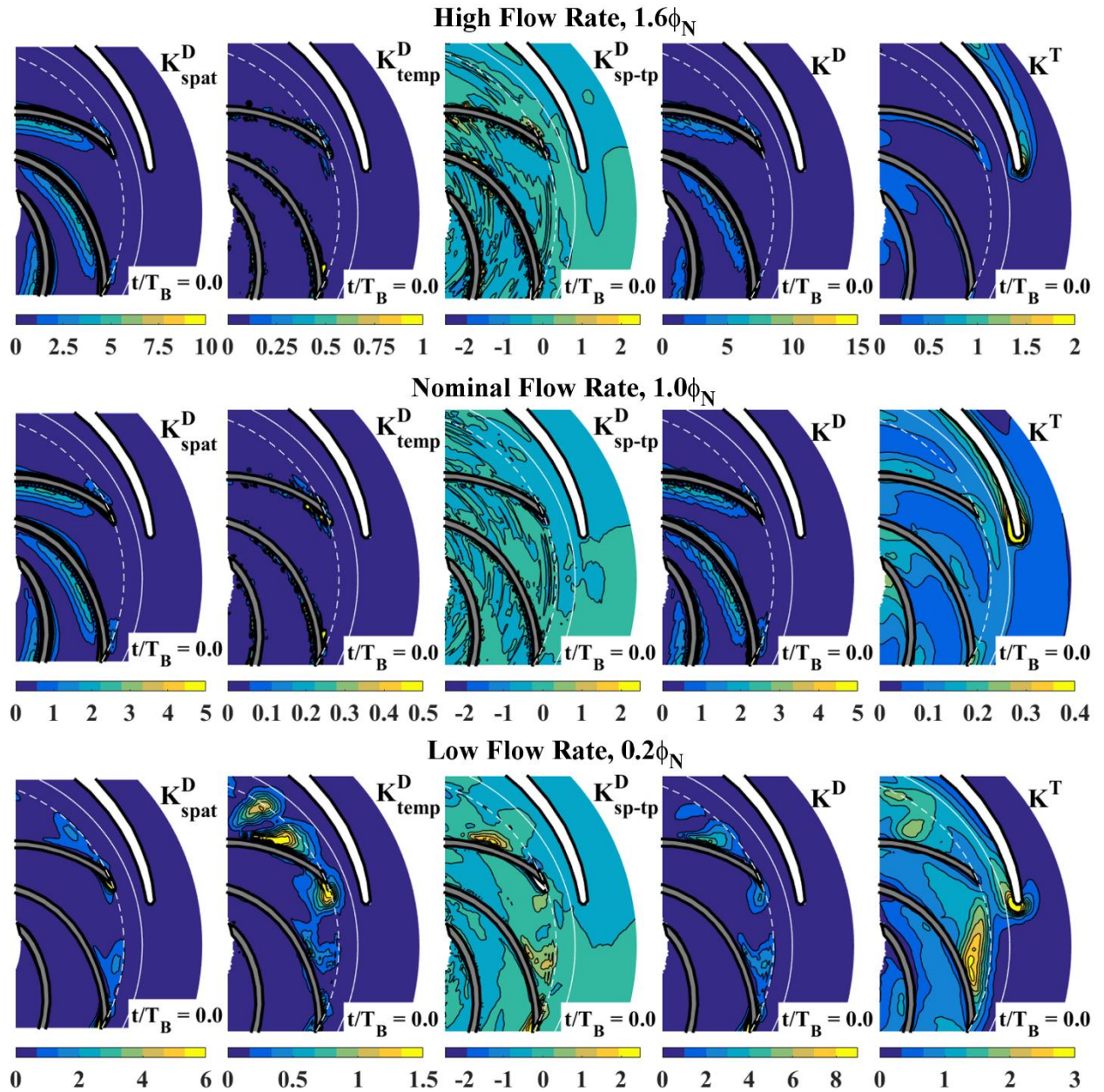**Fig. 11. Distribution of the temporal correlation of the DKE as a function of the flow rate.**

Fig. 12. Distribution of the spatial-temporal correlation of the DKE as a function of the flow rate.

Fig. 13. Distribution of the pitch-averaged spatial correlation of the DKE as a function of the flow rate.

Fig. 14. Comparison of instantaneous fluctuations related to deterministic (identifying correlations) and turbulent mechanisms as a function of the flow rate: highest (top), nominal (middle) and lowest (bottom) flow conditions.